ENSEMBLE-BASED ANALYSIS OF THE 14 JUNE 2010 OKLAHOMA CITY FLOOD

Nathan A. Dahl, Ming Xue, Fanyou Kong, Kevin Thomas, Yunheng Wang, and Keith Brewster
Center for Analysis and Prediction of Storms, Norman, OK

1. Introduction

Extreme rainfall events come in a variety of forms with a variety of contributing factors. Forcing mechanisms for persistent convection over a given area include relatively long-lived processes such as steady flow over complex terrain, large-scale ascent from synoptic forcing, or tropical cyclones approaching land (Heideman and Fritsh 1988). An added degree of difficulty lies in attempting to forecast extreme rainfall events driven primarily by mesoscale convective processes and transient features such as outflow boundaries. Clark et al. (2010a) noted from previous studies that, while convection-parameterizing models have difficulty depicting the key processes involved in the development and maintenance of mesoscale convective systems (MCSs) often responsible for flooding rains, a deterministic model operating at convection-allowing scales is plagued by rapid growth of errors stemming from insufficient data sampling and the chaotic unresolved behavior of small-scale convection.

These difficulties have motivated emphasis on probabilistic techniques employing forecast ensembles, such as the Storm Scale Ensemble Forecasts (SSEF) produced by the Center for Analysis and Prediction of Storms (CAPS; see Xue et al. 2010). When model and observation uncertainties are adequately represented by the ensemble distribution, ensemble methods have been shown to generally improve the reliability of probabilistic forecasts of mesoscale convective phenomena, particularly when the ensemble is run at convection-allowing resolution (Clark et al. 2009). This improvement is illustrated in the SSEF forecast of the 14 June 2010 extreme rain event in central Oklahoma, which substantially outperformed operational models and convection-parameterizing ensembles. This paper examines that case by grouping SSEF members by forecast skill and then comparing forecast fields of members from different skill groups to isolate mesoscale and convective-scale processes responsible for the event.

* *Corresponding Author's Address*: Nathan Dahl, Center for Analysis and Prediction of Storms, 120 David L. Boren Blvd., Suite 5900, Norman, OK, 73072.
E-mail: dahl_nathan@ou.edu

The CAPS SSEF is a 4-km ensemble, with an additional 1-km deterministic forecast included for comparative purposes. Ensemble distributions for a variety of diagnostic parameters and forecast variables, including reflectivity and accumulated precipitation, are processed from the SSEF output and made available in real-time. Along with the ensemble mean and maximum, neighborhood probability and probability-matched mean were computed to circumvent the "smearing" effect of simple ensemble averaging (Xue et al., p.2). Ebert (2001) found that this method improved forecast skill for a "poor man's ensemble" of seven operational NWP models, and Xue et al. likewise found that it improved substantially on those of the operational NCEP NAM or SREF for a number of mesoscale-driven heavy rain events during the 2010 Spring Experiment, including the June 14 Oklahoma City flooding event described here. (See Xue et al., Figure 6.)

As of 2010, the CAPS ensemble consisted of 19 WRF-ARW members, 5 WRF-NMM members, and 2 ARPS members; the characteristics of each model group are summarized in Xue et al. 2010 (pp. 5-6). The variety of model configurations is essential to enable the ensemble envelope to capture the behavior of any of the possible convective modes encountered in a given forecast period. Previous research has used this variety to diagnose factors responsible for the evolution of mesoscale convective events; for example, Schumacher et al. (2013) used neighborhood-based Equitable Threat Score (ETS; see Clark et al. 2010b) to rank the overall skill of the various ensemble members in forecasting a slow-moving mesoscale convective vortex. The results enabled them to efficiently isolate patterns relating member settings and treatment of features of interest to model skill; therefore, similar methods were employed for this study.

2. Overview of the 14 June 2010 Oklahoma City Flood

Under the influence of entrenched high pressure to the east and a slow-moving, vertically-stacked cutoff low to the west, the Southern Plains received sustained deep moisture advection from the Gulf of Mexico from late 11 June through late 13 June. A broad region of moderate instability with high precipitable water content resulted, with late-afternoon CAPE values on 13 June generally ranging from 2000 to 3000 J kg^{-1} across the region. At the same time, outflow from a series of MCSs in the Central Plains produced a stationary boundary extending from the Great Lakes region into the Texas and Oklahoma Panhandles. (See Figure 1.)

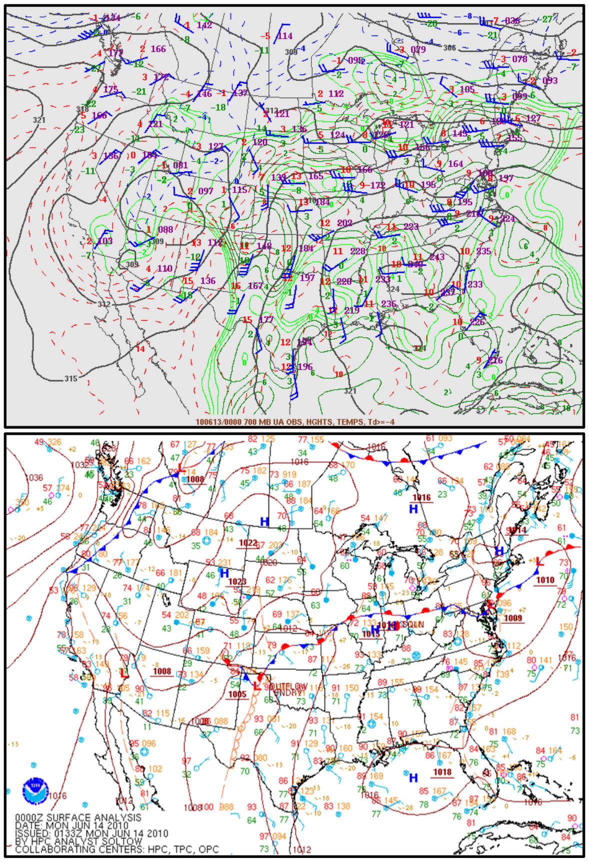

Figure 1: (top) Contoured 700 mb height (solid black), temperature (red dashes), and dewpoint (solid green) at 0000 UTC, 13 June 2010. (bottom) HPC surface analysis for 0000 UTC, 13 June 2010. (from the Storm Prediction Center severe weather archive)

The intersection of the outflow boundary and a dryline extending southward into west-central Texas provided a focus for organized convection in the afternoon and evening of 13 June, which produced an eextensive cold pool that propagated into north-central Oklahoma early on the morning of 14 June. Ahead of the cold pool, the 1200 UTC OUN sounding showed an uncapped, moderately unstable air mass with a precipitable water content of over 50 mm. Moreover, a strong nocturnal low-level jet had developed at a large angle to the expected orientation of the outflow boundary, with south-southwesterly 850 mb winds approaching 20 m s^{-1} and little speed or directional shear evident in the midlevels. (See Figure 2.) These ingredients indicated a “textbook” environment for a heavy rain event.

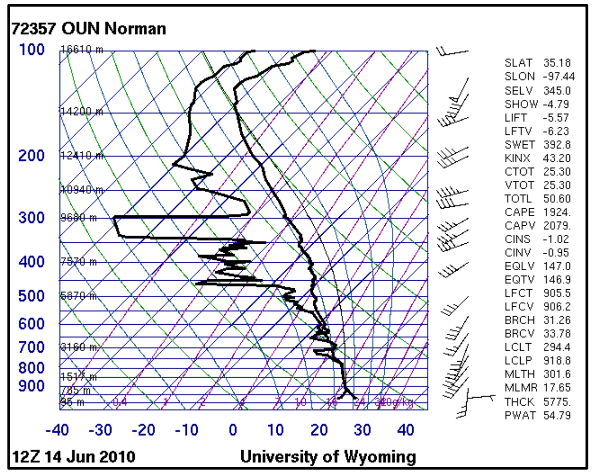

Figure 2: OUN Sounding for 1200 UTC, 14 June 2010. (from the University of Wyoming sounding archive)

Analysis by Basara et al. (2011) indicated that the manner in which the leading edge of the cold pool progressed through central Oklahoma was critical to the development of extreme precipitation in the Oklahoma City area early on 14 June. Analysis of cold pool propagation is often hindered by lack of resolution in surface station observations; fortunately, this particular event occurred in a region well-sampled by both the Oklahoma Mesonet and the WSR-88D radar network. Figure 3 shows that the outflow boundary initially curved from an east-west orientation on the southern flank to a more north-south orientation near the leading edge. At this point, conditions resembled the “mesohigh event” flash flood model diagrammed by Maddox et al. (1979) in many respects, although there were significant differences as well; for example, Maddox et al. prescribe a nearby midlevel ridge axis, substantial midlevel directional shear, and steering winds oriented parallel to the outflow boundary for mesohigh events, none of which were present in this case.

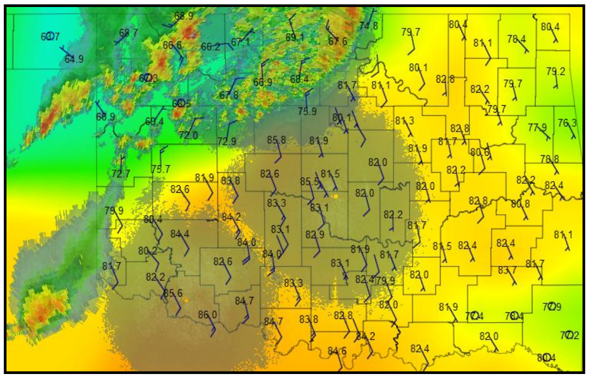

Figure 3: WSR-88D reflectivity mosaic overlaid on 0330 UTC 1.5 m AGL temperature (color gradient in Fahrenheit) and wind (barbs in kts) observations from the Oklahoma Mesonet.

In the hours preceding the onset of sustained heavy rain in Oklahoma City, the eastern portion of the cold pool advanced rapidly southeastward while the western portion stalled near the I-40 corridor. This along-line variation reoriented the outflow boundary just southwest of Oklahoma City to a direction almost perpendicular to the low-level jet indicated by Figure 2. At the same time, a weaker, meridionally-oriented outflow boundary from isolated convection approached from the southwest, stalling in the vicinity of I-44. As a result, a corridor of moist, uncapped, conditionally-unstable air developed directly upstream from Oklahoma City as the event unfolded, bordered by a convergence zone to the west and a region of maximized low-level isentropic ascent to the north/northeast.

Figure 4 shows bands of convection initially forming upstream of the region of maximized ascent and rapidly intensifying as they approached Oklahoma City, organizing by 1200 UTC into a small but vigorous backbuilding, quasi-stationary MCS. The method detailed in Corfidi et al. (1996) for predicting the motion of the MCS core indicates near-cancellation of the advection and propagation components, with a predicted motion of 2.6 m s^{-1} from the NNE. Rather than moving over the cold pool and losing intensity, this new MCS remained largely in phase with the outflow boundary (with both moving very slowly) for several hours; this phase relationship appears to have further intensified the new cells feeding into the southwest flank. As a result, Mesonet sites in the Oklahoma City area recorded average rainfall rates of over an inch an hour for the six-hour period from 0900 to 1500 UTC. (See Figure 5.)

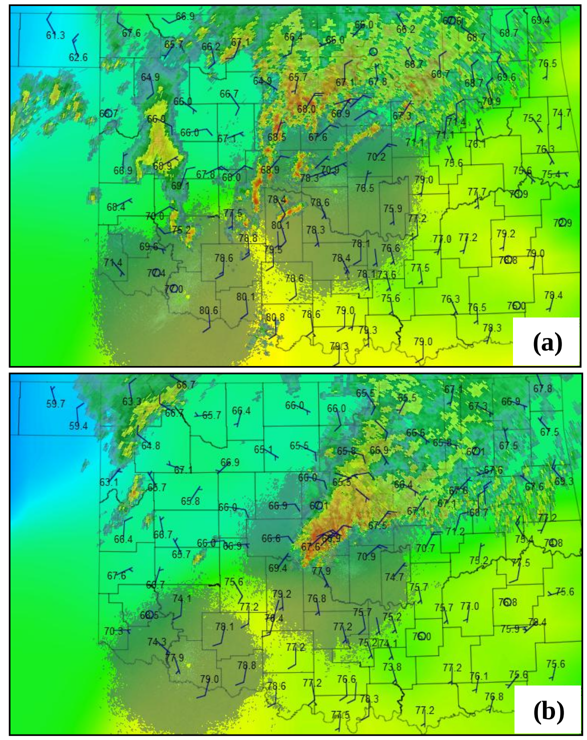

Figure 4: Same as Figure 2, but valid at 0830 (a) and 1030 UTC (b).

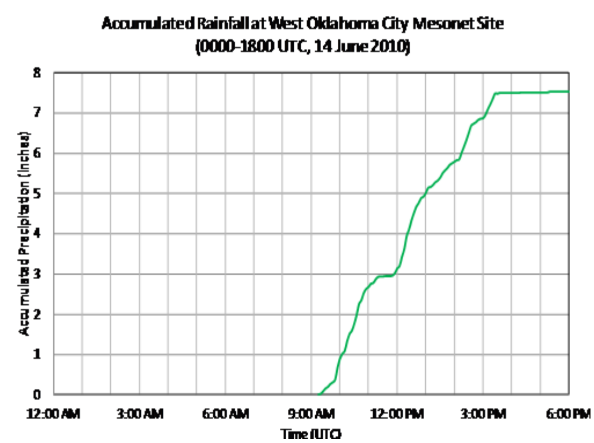

Figure 5: Rainfall accumulation (in) at OKCW Mesonet site vs. time (UTC) for 14 June 2010.

3. Data and Methods

The CAPS SSEF output for this event was examined to identify the features that were most significant for the development of the MCS responsible for this event. A direct comparison of the three-dimensional forecast states for all 26 ensemble members was deemed intractable in this study due to uncertainties associated with the impact of physics differences intrinsic to individual members. (For example, the Goddard shortwave radiation scheme was used for all of the ARW members but none of the NMM members.) Since the NMM and ARPS members generally demonstrated less QPF over the course of the Spring Experiment (Xue et al. 2010), they were excluded from further analysis

The QPF skill of each ARW member was evaluated using Stage-IV hourly accumulated precipitation fields assessed by the National Center for Environmental Prediction (Lin and Mitchell 2005). As noted in Clark et al. (2010b), a simple point-by-point verification of a precipitation forecast is not a good indicator of model skill since small spatial errors incur large penalties, particularly for intense precipitation. A neighborhood-based verification approach similar to theirs was employed here. In this approach, correct negatives and misses are assessed point-by-point, but hits and false alarms are assessed using a specified neighborhood radius.

To use this method, the forecast and observation locations must be collocated. The gridded hourly precipitation accumulations from the 18-hour period encompassing the event (i.e. from 0000 to 1800 UTC) for each ARW member were mapped to the Stage-IV grid locations using bilinear interpolation. Threat scores were calculated using an hourly accumulation threshold of 10mm and a neighborhood radius of 25 km over the domain illustrated in Figure 6. As a shorthand method of obtaining preliminary rankings for the ensemble members, the scores were also aggregated over the 18-hour forecast period.

Verification of forecast surface conditions was performed using archived observations from the Oklahoma Mesonet. The positions of the observed and forecast outflow boundaries over western Oklahoma from 0500 to 1400 UTC were objectively analyzed by mapping the Mesonet temperature observations to the ARW grid using a two-pass Barnes analysis, smoothing out impacts of isolated convection ahead of the boundary using a top-hat filter of radius 25 km, and then using prior knowledge of boundary orientation to identify the position along each meridional slice in Region A of the ARW grid. The line-averaged bias and root mean square error (RMSE) in north-south boundary position were then computed at hourly intervals.

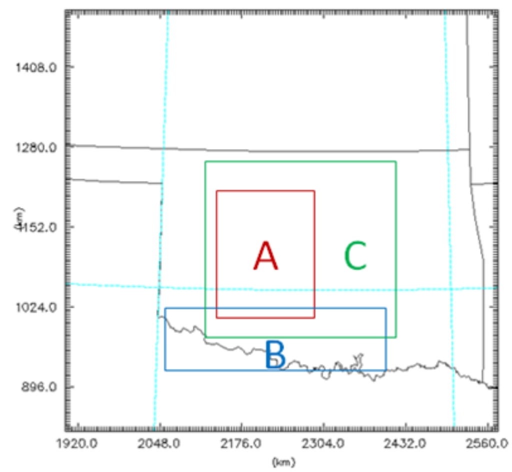

Figure 6: Region of the ARW model output used for initial QPF ETS calculations, along with regions used for outflow boundary verification (red), verification of surface and upper-air conditions (blue), and event-intensive ETS calculations (green). *x* and *y* coordinates are distances from the model grid origin (km).

Additionally, the forecast 2 m temperature and dewpoint fields were interpolated to the Mesonet station locations within Region B of Figure 6 and used to calculate warm-sector bias and RMSE at hourly intervals for each of the ARW members. Simple bivariate correlations between QPF skill and these aspects of the near-surface forecasts were assessed using Pearson coefficients. Similar correlations were sought between pertinent upper-air conditions in Region B and QPF skill. Finally, after the influence of model settings on these metrics was inferred, high-skill and low-skill members were qualitatively compared to identify specific phenomena produced only by the high-skill members near the region of interest.

3. Results and Discussion

a. Statistical analysis relating near-surface conditions to QPF skill

The hourly QPF threat scores for the 10mm threshold are plotted in Figure 7, while the accumulated 10 mm threat scores from 0000 to 1800 UTC are ranked in Table 1. First, both the plots and

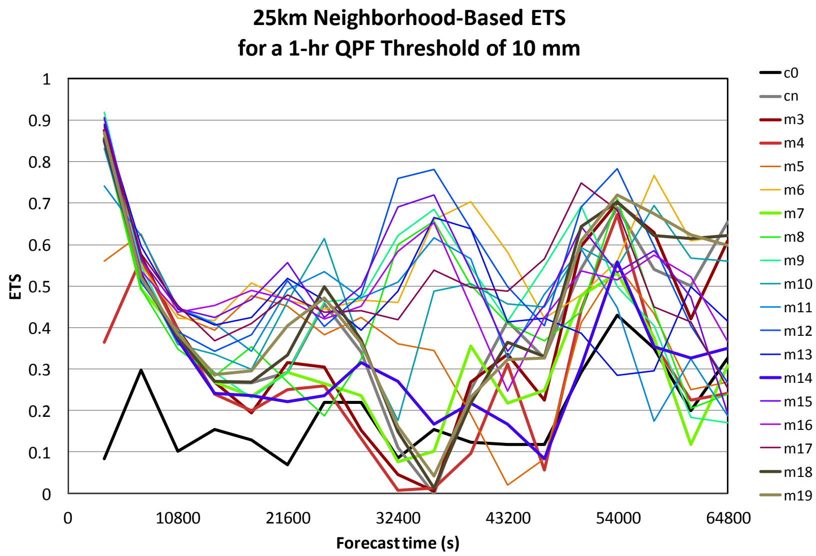

Figure 7: Hourly QPF threat scores for full domain shown in Figure 6 using an hourly accumulation threshold of 10 mm. Bold lines indicate plots for SSEF members employing the Thompson microphysics scheme.

Table 1. ARW members ranked by 10 mm hr^{-1} QPF ETS aggregated from 0000 to 1800 UTC 14 June 2010 for the full domain in Figure 6. Characteristics of each member (PBL and land surface model parameterizations and initial and boundary conditions) are listed at right.

RANK	MEMBER	ETS	Microphysics	PBL	LSM	IC	BC
1	arw_m15	0.5243	WDM6	MYJ	Noah	00Z ARPSa	00Z NAMf
2	arw_m6	0.5223	Morrison	YSU	RUC	cn – em-p1_pert	21Z SREF em-p1
3	arw_m12	0.5192	WDM6	QNSE	RUC	cn+etaKF-p1_pert	21Z SREF etaKF-p1
4	arw_m16	0.4904	WSM6	MYJ	Noah	00Z ARPSa	00Z NAMf
5	arw_m17	0.4852	Morrison	MYJ	Noah	00Z ARPSa	00Z NAMf
6	arw_m13	0.4837	WSM6	QNSE	Noah	cn – etaBMJ-n1_pert	21Z SREF etaBMJ-n1
7	arw_m11	0.4701	Ferrier	YSU	Noah	cn – etaKF-n1_pert	21Z SREF etaKF-n1
8	arw_m9	0.4553	WDM6	MYNN	Noah	cn + nmm-p2_pert	21Z SREF nmm-p2
9	arw_m10	0.4438	Ferrier	YSU	RUC	cn + rsmSAS-n1_pert	21Z SREF rsmSAS-n1_pt
10	arw_m8	0.4175	WSM6	QNSE	RUC	cn – nmm-p1_pert	21Z SREF nmm-p1
11	arw_m19	0.4043	Thompson	MYNN	Noah	00Z ARPSa	00Z NAMf
12	arw_m18	0.3933	Thompson	QNSE	Noah	00Z ARPSa	00Z NAMf
13	arw_m5	0.3867	Morrison	YSU	RUC	cn+em-p1+recur pert	21Z SREF em-p1
14	arw_cn	0.3766	Thompson	MYJ	Noah	00Z ARPSa	00Z NAMf
15	arw_m3	0.3428	Thompson	MYJ	Noah	cn + random pert	00Z NAMf
16	arw_m7	0.3069	Thompson	QNSE	Noah	cn+em-p2_pert	21Z SREF em-p2
17	arw_m14	0.3062	Thompson	MYNN	RUC	cn + etaBMJ-p1_pert	21Z SREF etaBMJ-p1
18	arw_m4	0.2632	Thompson	MYJ	Noah	cn + RF-smoothed pert	00Z NAMf
19	arw_c0	0.1944	Thompson	MYJ	Noah	00Z ARPSa	00Z NAMf

the ranked scores make it clear that the performance of the control ARW member with no radar data assimilation (arw_c0) was easily the worst. The importance of the initial radar data is illustrated in Figure 8; arw_c0 was much too slow in developing organized convection late on 13 June, which in turn adversely affected the forecast of the cold pool that clearly played a critical role in this event.

When examining the SSEF member attributes in Table 1 further, the most obvious pattern is the predominance of the Thompson microphysics scheme (Thompson et al. 2004) in the lower-scoring members, regardless other model attributes; eight of the nine lowest rankings were occupied by the members that used the Thompson scheme. Those members are plotted in bold in Figure 6, and their comparative lack of skill was concentrated in the period encompassing most of the observed rainfall in Oklahoma City.

Reviewing the member attributes in Table 1, a direct illustration of the impact of the Thompson scheme may obtained by comparing the forecasts of the arw_cn and arw_m15 members (which only differed in that the former used the Thompson scheme while the latter used the six-species double-moment WRF scheme described by Lim and Hong (2010)). Figure 9 shows that the Thompson scheme's treatment of cold pool development for the initial convection in northwest Oklahoma differed markedly from that of the WDM6 scheme within an hour of model initialization; the WDM6 cold pool is deeper, broader, and characterized by lower equivalent potential temperature. As was the case when initial radar data was not assimilated, the initial underestimate of cold pool strength resulted in outflow boundary placement errors that persisted for most of the event.

Because the large ensemble spread in outflow boundary positions became the dominant factor in temperature and dewpoint variations in Region B after 1200 UTC, temperature and dewpoint bias and RMSE were calculated only for the first 12 hours of the forecast. The choice of PBL and LSM

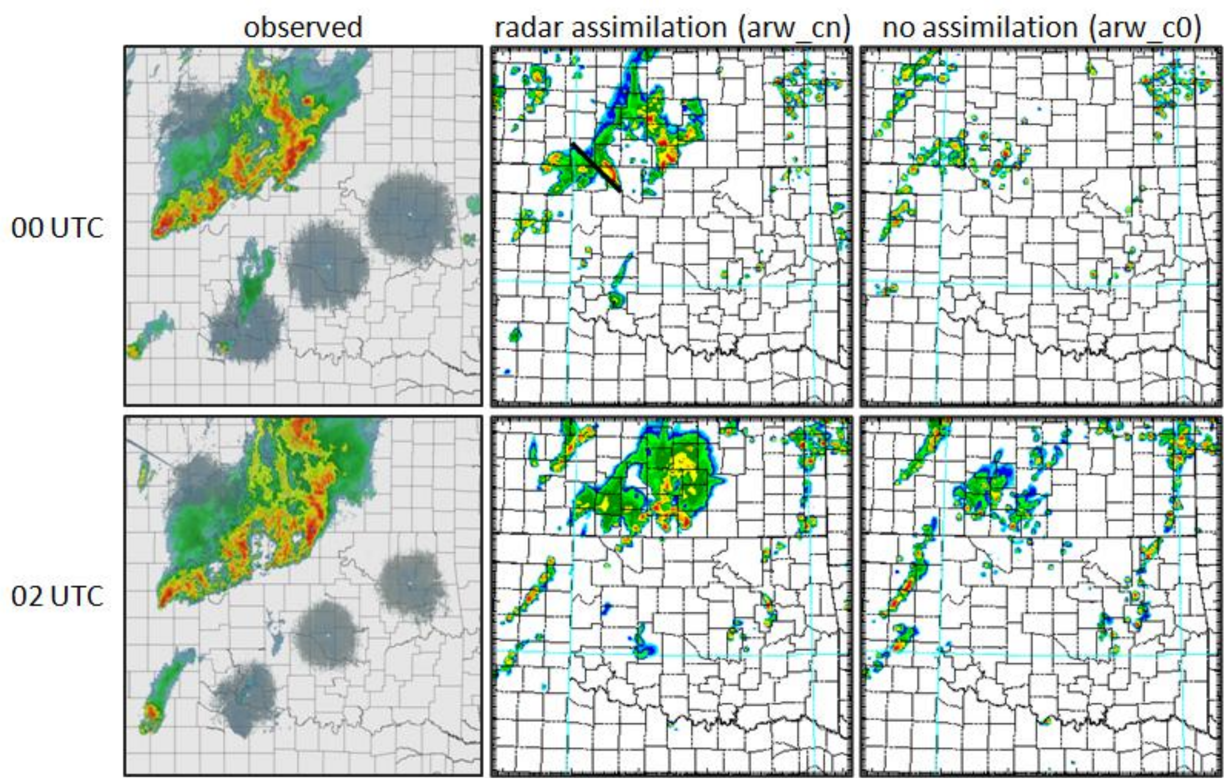

Figure 8: Observed radar reflectivity at 0000 (top) and 0200 UTC 14 June (bottom), compared with corresponding simulated reflectivity from ARW control members with and without assimilation of initial radar data. Solid black line shows the position of the vertical cross section used for Figure 8.

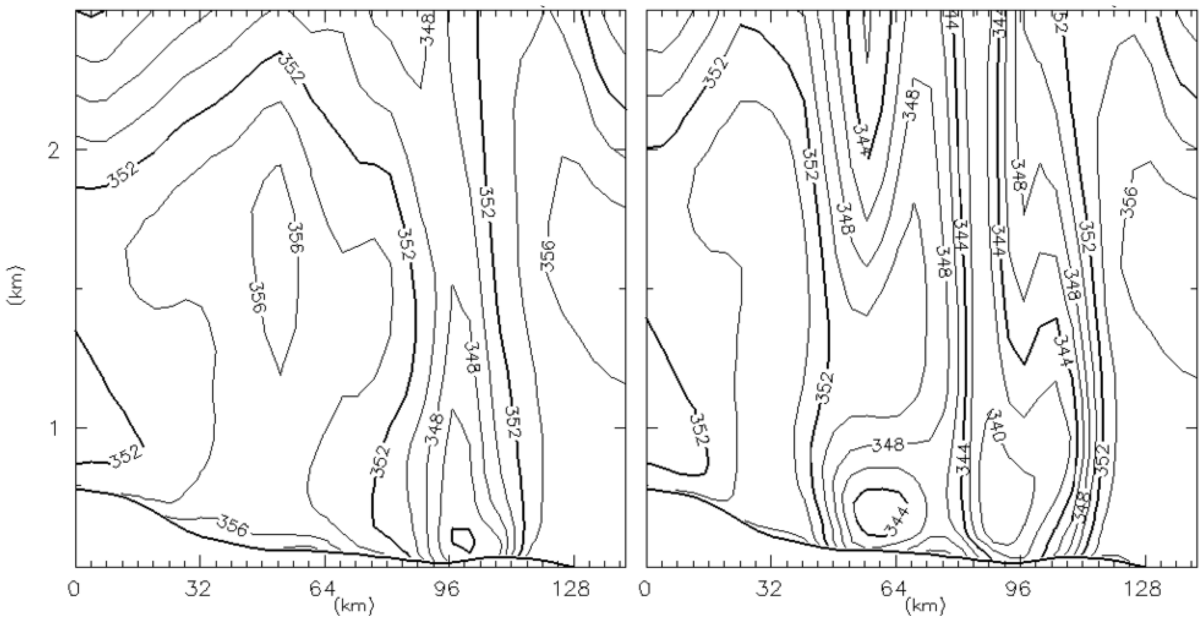

Figure 9: Equivalent potential temperature within vertical cross section taken along the black line in Figure 8 for arw_cn (left) and arw_m15 (right) one hour after initialization.

schemes impacted the forecast surface conditions noticeably (e.g. with comparatively warmer and drier conditions from the YSU scheme after a few hours, agreeing with the results in Hu et al. 2010). However, Table 2 suggests that these variations were not as important as outflow boundary placement for increasing QPF skill for this event; with Pearson coefficients (r) calculated for the period from 0600 to 1200 UTC, the values are much lower for the Region B surface forecast errors than they are for the outflow boundary position bias and RMSE, even with a two-hour time lag applied to maximize the correlation.

Table 2: Pearson correlation coefficients relating surface condition statistical parameters to QPF forecast skill from 0600 to 1200 UTC, 14 June 2010

PARAMETER	r (10mm 1-hr QPF)	r (20mm 1-hr QPF)
Temperature Bias	0.10	0.09
Temperature RMSE	0.13	0.12
Dewpoint Bias	-0.04	-0.26
Dewpoint RMSE	0.02	-0.20
OFB Position Bias	-0.70	-0.56
OFB Position RMSE	-0.74	-0.62

b. Statistical analysis relating upper-air conditions to QPF skill

The sounding in Figure 2 depicts four key features associated with the event: a low-level jet with a strong meridional component; exceptionally high precipitable water content; substantial CAPE; and a lack of CINH. For the low-level jet, the ensemble member depictions of the average meridional 850 mb wind speed in Region B were investigated. Small systemic differences were noted (e.g. a slightly reduced diurnal cycle for the low-level jet from the YSU PBL members, a stronger nocturnal jet from the Noah LSM members). However, the correlation between these differences and variations in subsequent QPF skill appears to be negligible, with r = 0.23 for the 10 mm threshold and 0.00 for the 20 mm threshold. Similarly, variations in forecast precipitable water did not appear to relate strongly to QPF skill (r = -0.21 for the 10 mm threshold and -0.25 for the 30 mm threshold).

Variations in surface-based CAPE (r = -0.24 for the 10 mm threshold and -0.57 for the 20 mm threshold) and CINH (r = -0.27 for the 10 mm threshold and -0.36 for the 20 mm threshold) appear to have been more of a factor. However, the implications for the skill of individual members are unclear; for example, the YSU members generally had less CAPE, but they also had less CINH early in the forecast period. The only other clear pattern relating model settings to CAPE and CINH is that arw_m4 and arw_m5 are clear outliers early in the period. (See Figure 10.) Reviewing Table 1, this appears to stem from the use of recursive filtered perturbations in the initial conditions for those members; as shown in Figure 11, these perturbations initiated widespread spurious convection in the domain that persisted for a few hours in some areas, artificially stabilizing the atmosphere and leading to errors in outflow boundary location similar to those seen in the members that employed Thompson microphysics.

c. Qualitative high-skill/low-skill comparison of convective features

Since the progress of the outflow boundary had the strongest correlation with QPF skill, and since the members that used the Thompson microphysics scheme and/or recursive filter perturbations for the initial conditions were without exception the worst at predicting outflow boundary position, those members were eliminated from further analysis. In order to focus on the timing, placement, and intensity of the

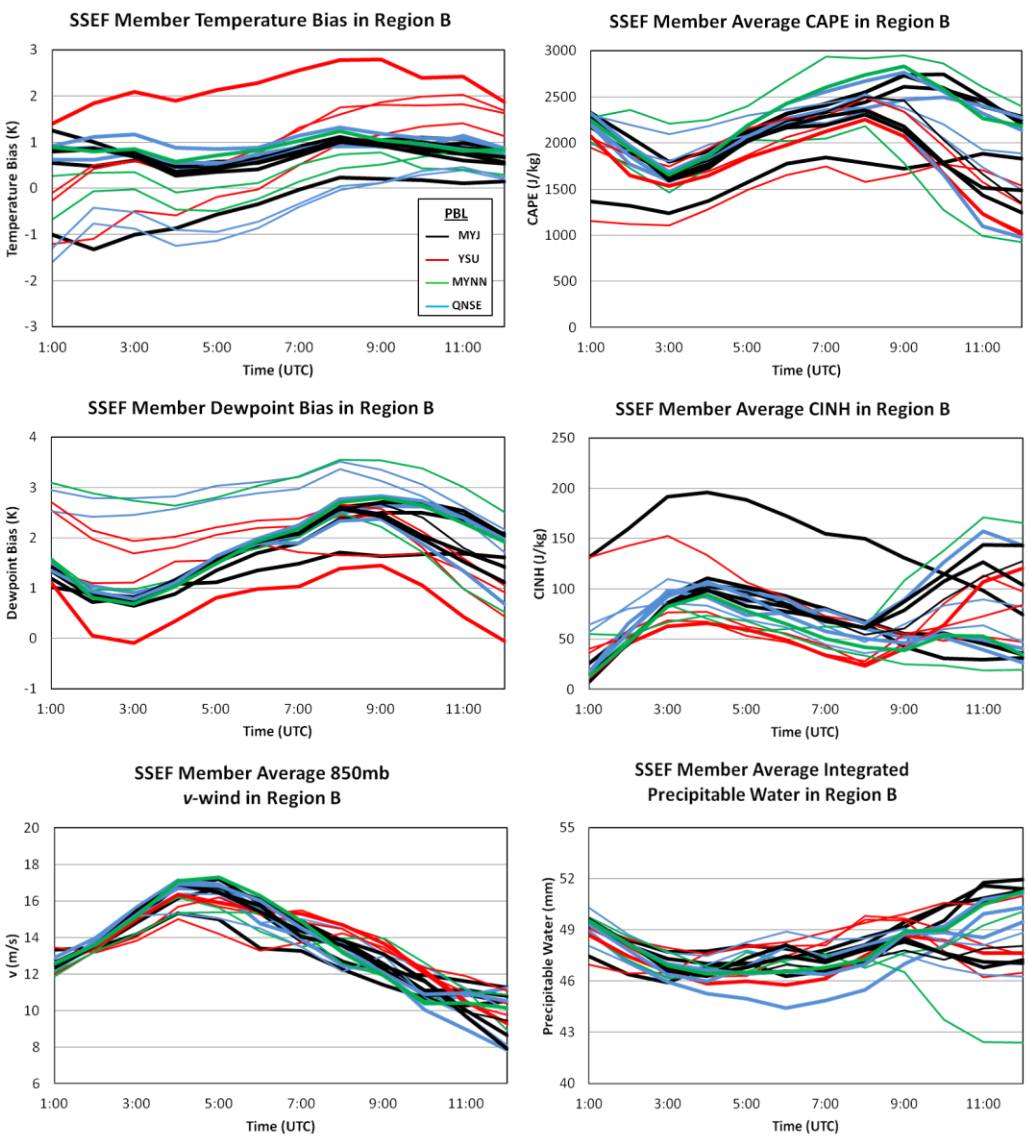

Figure 10: Hourly temperature bias (K), average CAPE (J kg^{-1}), dewpoint bias (K), average CINH (J kg^{-1}), average 850 mb meridional wind speed (m s^{-1}) , and average precipitable water (kg m^{-2}) in Region B of Figure 6. Members using the Noah LSM scheme are plotted in bold. (Note the two stable outliers in the CAPE and CINH plots, corresponding to members arw_m4 and arw_m5.)

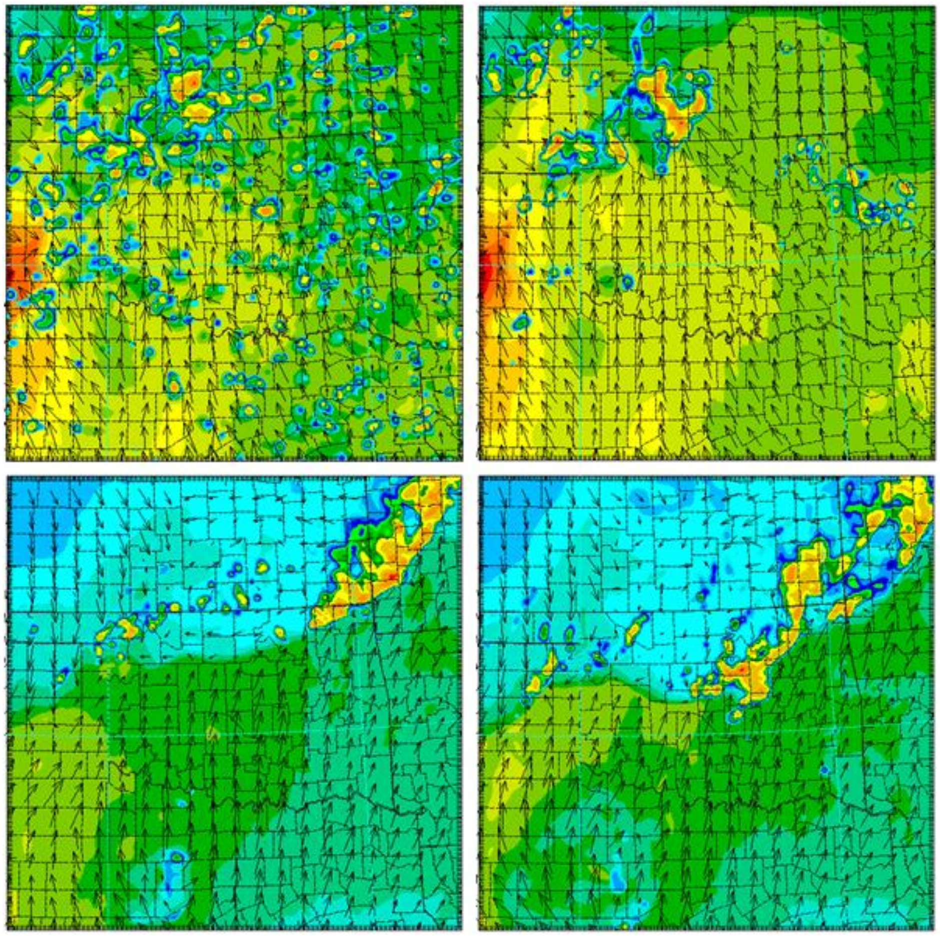

Figure 11: Simulated near-surface reflectivity and wind vectors overlaid on surface potential temperature at 0100 (top) and 0900 (bottom) UTC for arw_m5 (left) and arw_m6 (right).

Table 3. ARW members ranked by 20 mm hr^{-1} QPF ETS aggregated from 0800 to 1500 UTC in Region C of Figure 6. Characteristics of each member are listed at right.

RANK	MEMBER	ETS	Microphysics	PBL	LSM	PVS RANK
1	arw_m9	0.614	WDM6	MYNN	Noah	8
2	arw_m12	0.567	WDM6	QNSE	RUC	3
3	arw_m6	0.559	Morrison	YSU	RUC	2
4	arw_m10	0.488	Ferrier	YSU	RUC	9
5	arw_m8	0.484	WSM6	QNSE	RUC	10
6	arw_m16	0.475	WSM6	MYJ	Noah	4
7	arw_m15	0.463	WDM6	MYJ	Noah	1
8	arw_m13	0.433	WSM6	QNSE	Noah	6
9	arw_m11	0.288	Ferrier	YSU	Noah	7
10	arw_m17	0.286	Morrison	MYJ	Noah	5

event itself, QPF skill was recalculated for the remaining members in Region C of Figure 6 for the period from 0800 to 1500 UTC using a 1-hour accumulation threshold of 20 mm. The results are shown in Table 3. Substantial changes resulted in the rankings; for example, arw_m8 and arw_m9 are much higher here than in Table 1, while arw_m15 and arw_m17 are much lower. This suggests that ranking model performance on the sole basis of a single calculation of QPF skill is not reliable.

Taking Table 1 and Table 3 in tandem, it is also unclear if there were any additional patterns relating model settings to skill. Therefore, further analysis focused on a qualitative comparison of convective phenomena produced by high-skill and low-skill members. In comparing the simulated reflectivity fields, the most consistent difference appears to be the development of strong cellular convection in the warm sector prior to the development of the backbuilding MCS for the higher skill members. (See Figure 12.) Similar to the observed convection noted in Figure 3a, the simulated warm-sector cells in the higher skill members initiated along a weaker boundary produced by earlier convection. (See Figure 13.)

The lower-skill members produced this boundary as well, but incipient cells decayed rapidly after moving off the boundary for those members. There was no clear difference between high-skill and low-skill members in the placement or strength of the low-level convergence at this time, so the crucial difference apparently concerned buoyancy rather than dynamic forcing. This conjecture is supported by the CAPE and CINH values listed in Table 4, derived from soundings extracted from the region circled in Figure 13b; the high-skill members universally predicted higher CAPE and lower CINH in the area. Taking the behavior of arw_m15 into account, cell growth was apparently tied in particular to lower CINH.

The importance of this convection to the evolution of the outflow boundary in central Oklahoma is demonstrated in Figure 14, which plots the difference in surface meridional wind between example high-skill and low-skill members. In the first pairing, where only the high-skill member produced substantial convection in the warm sector early on, the difference field develops a “braided” appearance after that convection merges with the outflow boundary, indicating an along-line variation in outflow boundary speed near the merge point. In the second pairing, in which both members (arw_m9 and arw_m15) produced warm-sector convection, the difference field shows a more consistent band of positive differences, indicating that the boundary in the low-skill member advanced more rapidly than that of the high-skill member all along the line.

Thus, the model representation of warm-sector convection appears to be linked to the model representation of the stalling and reorientation of the boundary associated with the rainfall event in Oklahoma City. Plots of the surface pressure fields for all ten members at 0600 UTC depict a mesohigh developing in northwestern Oklahoma, behind a convective line associated with the earlier MCS. This feature propagated into central Oklahoma by 1000 UTC, where it was reinforced by the warm-sector convection moving in from the southwest in the high-skill members and arw_m15. (See Figure 12.) At the same time, a band of dry subsidence (possibly associated with the entrance region of the 700 mb jet) developed to the west, accompanied by lower pressure and marginally warmer temperature at the surface. This had the dual impact of increasing the speed of the outflow boundary near the mesohigh while slowing outflow boundary progress to the west through weakened frontogenesis compounded by stronger heading winds associated with the synoptic-scale low to the southwest. This reoriented the outflow boundary at a larger angle to the low-level jet, locally enhancing lift. These factors triggered the development of a new, quasi-stationary convective cluster rooted to the outflow boundary between the mesohigh and the subsidence region.

Precipitation from this cluster continued to reinforce the mesohigh through evaporative cooling, and the configuration remained in place as long as dry subsidence and attendant low pressure persisted over the western portion of the boundary. The importance of this subsidence is illustrated in Figures 15 and 16; arw_m8 and arw_m9, which maintained dry regions over the western portion of the outflow boundary (circled areas) around 1000 UTC, showed persistent favorable outflow boundary reorientation during the event. arw_m12 and arw_m15, on the other hand, developed widespread spurious rainfall over western Oklahoma by 1000 UTC; attendant cooling and pressure rises drove the western portion of the boundary farther to the south, producing a less favorable orientation and causing much of the subsequent precipitation to fall to the south and/or east of the correct location in the case of arw_m15. arw_m12 presents an interesting case, earning a high QPF threat score despite flaws in its treatment of the

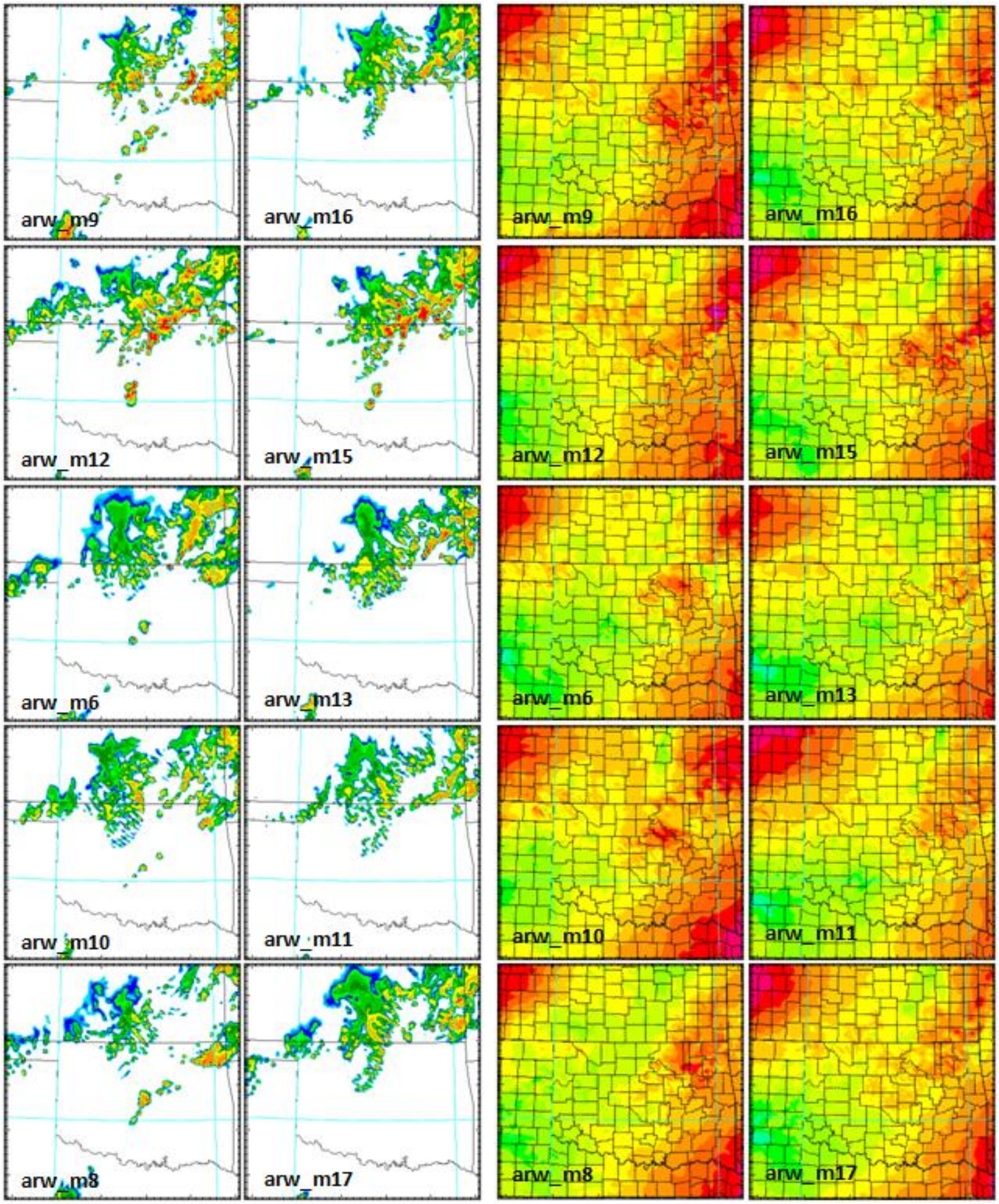

Figure 12: Forecast reflectivity at 0700 UTC (left) and surface pressure at 1000 UTC (right, with warmer colors indicating higher pressure) for high-skill (left column) and low-skill (right) members, shown from top to bottom in order of QPF ETS as shown in Table 3.

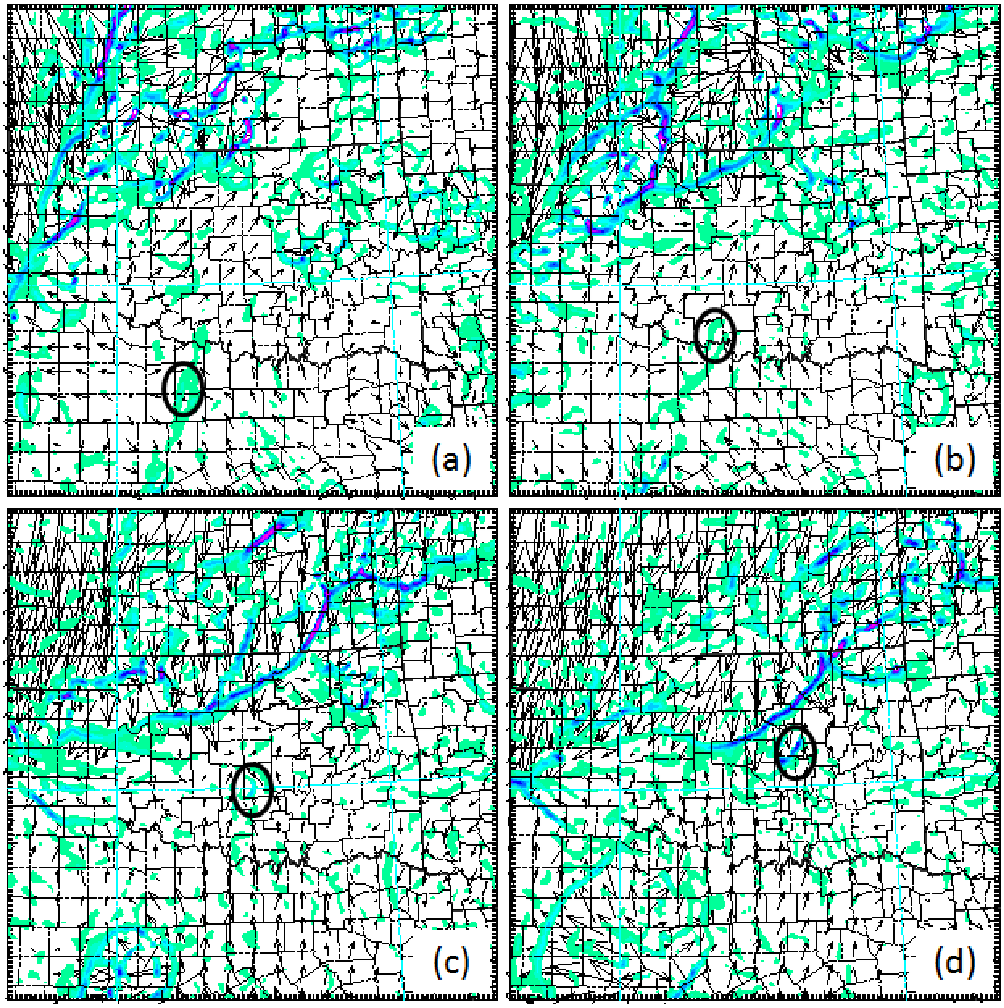

Figure 13: Horizontal convergence and perturbation wind vectors at roughly 250m AGL valid 0200 (a), 0400 (b), 0600 (c), and 0800 UTC (d) for member arw_m6. A region of convergence associated with pre-boundary convection is highlighted by the black circles.

Table 4. Convective instability and inhibition at the location circled in Figure 14b valid at 0400 UTC June 14, as derived from forecast soundings. (The members are listed in order of descending ETS rank using the scores from Table 3.)

MEMBER	CAPE (J kg^{-1})	CINH (J kg^{-1})
arw_m9	1017	12
arw_m12	1480	86
arw_m6	1120	112
arw_m10	1183	133
arw_m8	1328	66
arw_m16	915	135
arw_m15	971	132
arw_m13	1002	146
arw_m11	865	171
arw_m17	977	166

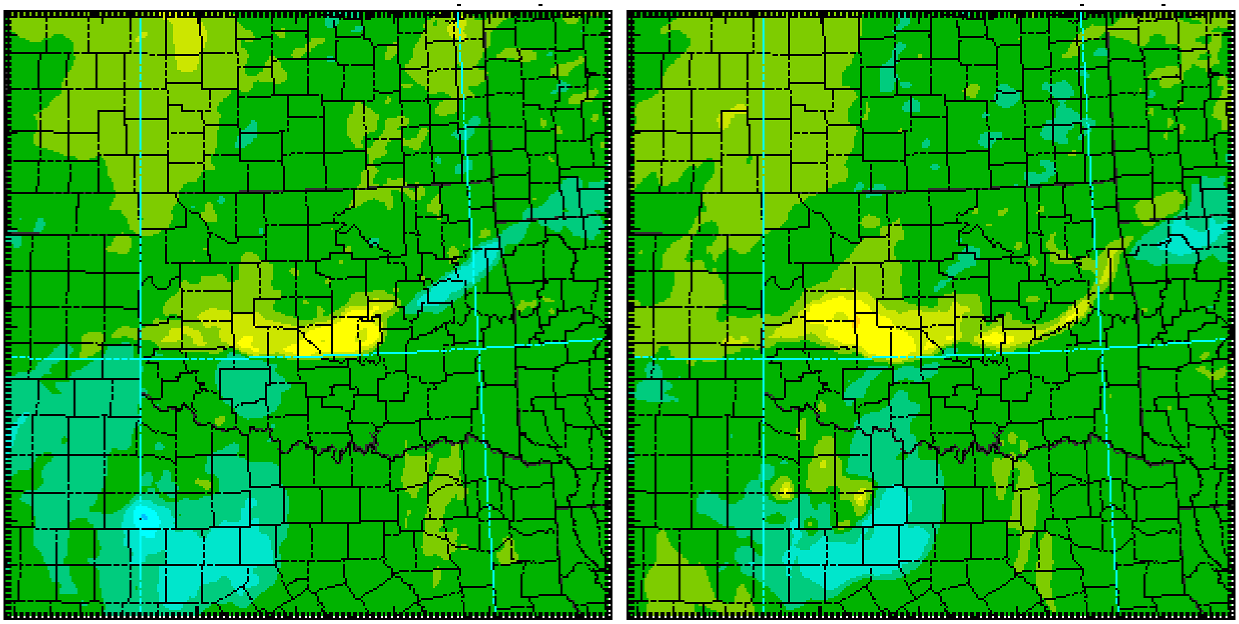

Figure 14: 1100 UTC surface potential temperature differences between high-skill member and low-skill member forecasts. Differences between arw_m8 and arw_m16 are plotted at left, while differences between arw_m9 and arw_m15 are plotted at right.

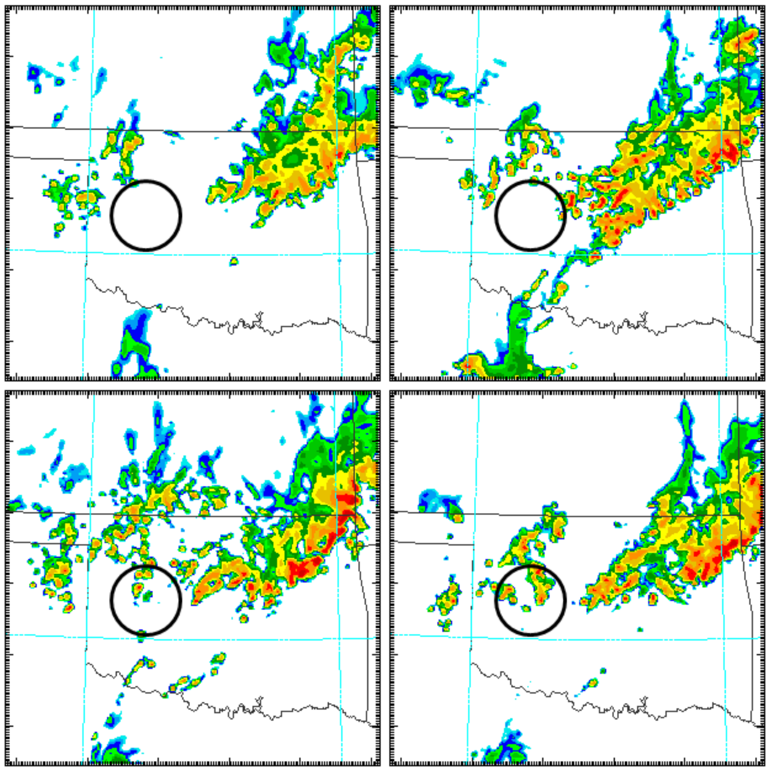

Figure 15: Reflectivity valid 1000 UTC for arw_m8 (upper left), arw_m9 (upper right), arw_m12 (lower left), and arw_m15 (lower right).

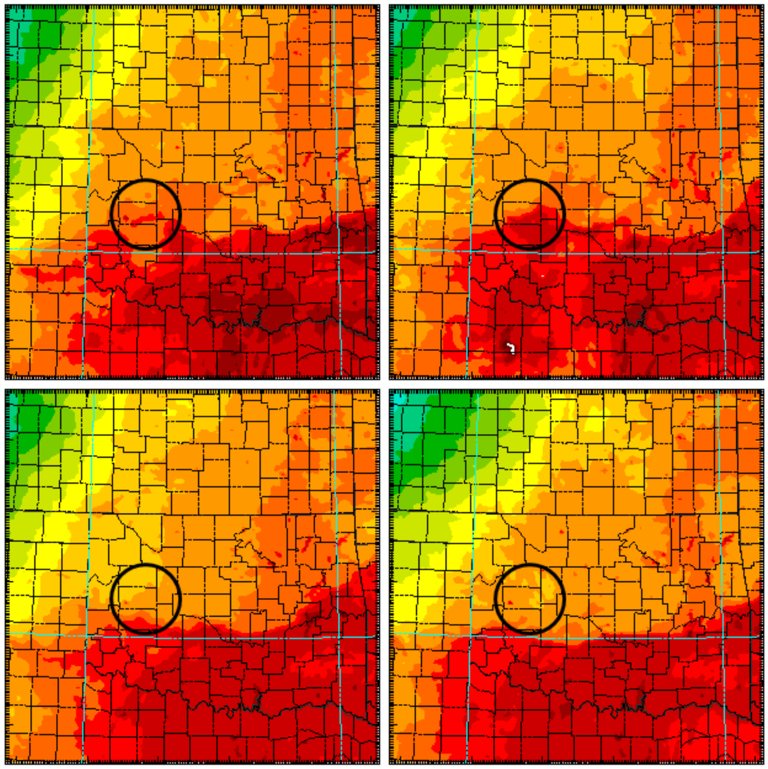

Figure 16: Same as Figure 16, but for surface temperature valid at 1200 UTC.

boundary. From inspection, it appears that the high score resulted from spurious widespread precipitation forming ahead of the boundary (perhaps due to an excess of CAPE as suggested by Table 4) but then tracking over the correct locations before dissipating. In brief, it appears that this member was "right for the wrong reasons."

A re-examination of the observed storm behavior reinforces the importance of the features examined above. Figure 17 depicts the observed reflectivity, temperature, and mean sea-level pressure as the event unfolded; by 0800 UTC, the earlier MCS had produced a mesohigh in north-central Oklahoma as isolated cells developed in the warm sector southwest of Oklahoma City. By 1000 UTC, those cells had coalesced into a new MCS over the reoriented boundary, with convective precipitation moving well away from the boundary and into the mesohigh. Meanwhile, a region of subsidence developed in the wake of the earlier storms, backing the winds behind the western part of the boundary and smothering additional cells moving in from the west. Shortly before 1200 UTC, the MCS entered an intense backbuilding phase that produced two inches of rain in western Oklahoma City over the next hour (see Figure 5), with an elongated plume of intense precipitation developing between the mesohigh and the subsidence region. However, at this time the subsidence region began to decay as the 700 mb jet max moved off to the northeast and cloud-layer winds behind the outflow boundary veered dramatically. After 1300 UTC, increasing rainfall developing on the western flank of the MCS gradually intensified the cold pool in central Oklahoma until the stalled portion of the outflow boundary was forced to the south and the event ended. Thus, the mesohigh, the subsidence region, and a tenuous balance of buoyancy and convective inhibition in the warm sector appear to have all been crucial factors in maintaining local rainfall intensity and duration in this case.

4. Summary and Conclusions

The backbuilding MCS responsible for the extreme rains and flooding observed in the Oklahoma City area on 14 June 2010 developed from a stalled front/mesohigh configuration similar to that detailed in Maddox et al. (1979) but altered in two key respects. First, an intense low-level jet overrunning a favorably-oriented segment of the outflow boundary combined with a lack of midlevel shear to produce a localized, vigorous MCS that remained nearly stationary for several hours. Second, subsidence to the west

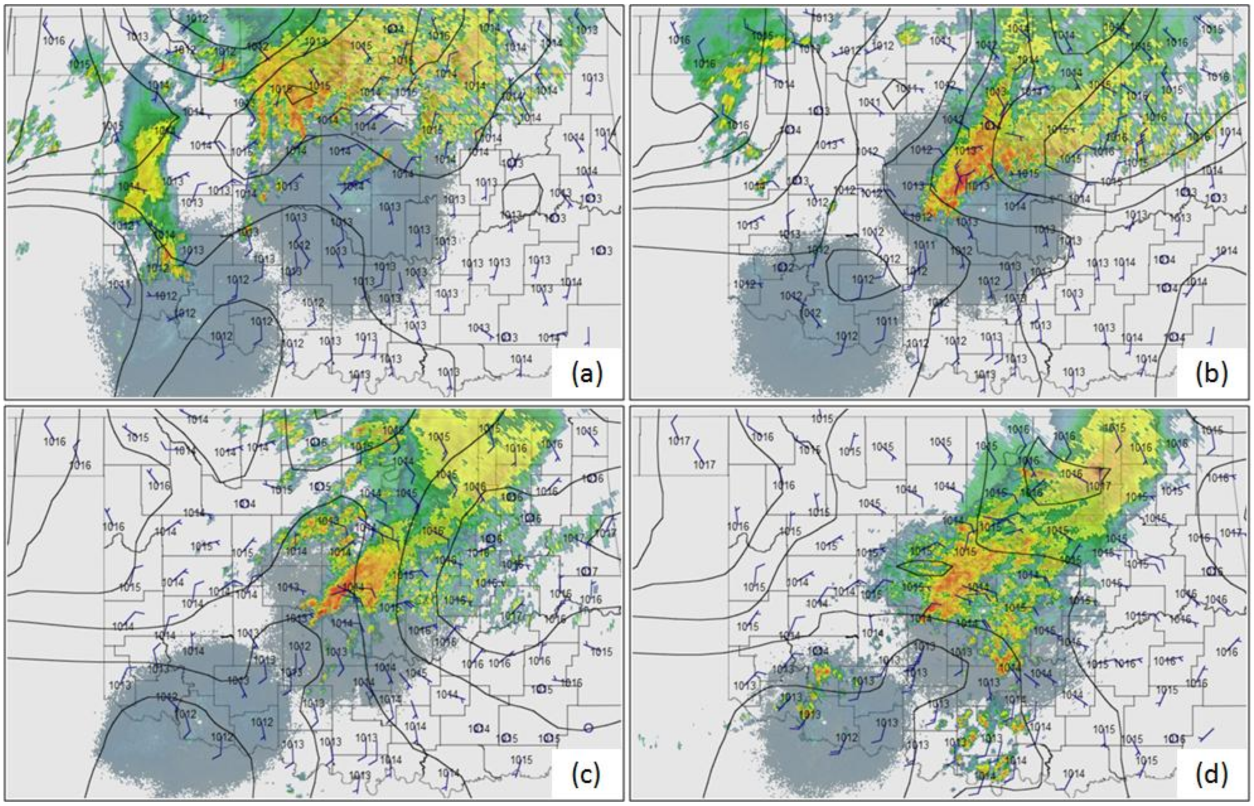

Figure 17: Observed mean sea level pressure (black contours, in mb) and winds with observed reflectivity mosaic overlaid, valid 0800 (a), 1000 (b), 1230 (c), and 1430 UTC (d).

(possibly synoptically-forced) initially helped orient the outflow boundary in a favorable manner and subsequently hindered additional cold pool development that would have driven the outflow boundary (and hence the MCS) out of central Oklahoma more quickly. The combination of the weak surface trough associated with this subsidence and a perpetual mesohigh to the east may also have played a role in maintaining and intensifying the MCS through low-level convergence, although this convergence is not definitively indicated by available observations.

The CAPS SSEF envelope captured these crucial features sufficiently to produce a highly skillful ensemble forecast of the extreme rainfall. In the process, errors tied specifically to the initialization procedure and parameterizations used for some of the members were brought to light. First, neglecting radar data assimilation severely diminished forecast quality from the outset. Second, using recursive filter perturbations in the initial conditions for this high-CAPE/low-CINH environment led to widespread spurious convection that persisted well into the forecast, similarly diminishing forecast quality. Finally, use of the Thompson microphysics scheme resulted in underestimation of initial cold pool strength and subsequent spread, possibly due to misdiagnosis of the drop-size distribution associated with the strong convection present at initialization. (The question remains as to whether this finding is specific to this case or an indication of an intrinsic limitation of the Thompson scheme; thus, a review of other cases in which the Thompson scheme was used to initialize environments containing strong warm-rain convection is recommended.)

Furthermore, the SSEF products suggested that minor variations in cold pool strength and warm sector buoyancy played substantial roles in determining the manner in which the event progressed. For instance, enough inhibition was required to keep convection and cold pool development isolated, but too much inhibition tended to produce an MCS that was too weak, too scattered, and unable to stall/backbuild in the correct location. Since it is unlikely that such variations would be reliably captured by a single deterministic forecast, this case provides further evidence for the superiority of ensemble-based methods in forecasting events of this sort.

Acknowledgements

This study was accomplished as part of a CAPS research assistantship advised by Dr. Ming Xue. CAPS ensemble forecasts were archived on the NICS High Performance Storage System and obtained and converted to ARPS format with technical assistance from Drs. Fanyou Kong and Yunheng Wang. Radar and *in situ* verification data were archived by the Oklahoma Mesonet and visualized using the WeatherScope software package. QPF verification data were obtained from the National Center for Environmental Prediction's Stage IV archive and mapped using online code (*http://www.emc.ncep.noaa.gov/mmb/ylin/pcpanl/QandA/sorc/gribplot.f*) provided by Mike Baldwin. The author thanks each of the individuals and entities listed above for providing their time and resources.

References

Basara, J. B., B. G. Illston, and G. D. McManus, 2011: Atmospheric contributors to the 14 June 2010 Flash Flood in Oklahoma City. Proceedings, *International Symposium on Earth-Science Challenges,* Norman, OK, University of Oklahoma and Kyoto University, ID 64.

Bryan, G. H., and H. Morrison, 2012: Sensitivity of a Simulated Squall Line to Horizontal Resolution and Parameterization of Microphysics. *Mon. Wea. Rev.*, **140**, 202–225.

Clark, A. J., W. A. Gallus, and M. L. Weisman, 2010a: Neighborhood-Based Verification of Precipitation Forecasts from Convection-Allowing NCAR WRF Model Simulations and the Operational NAM. *Wea. Forecasting*, **25**, 1495–1509.

Clark, A. J., W. A. Gallus, M. Xue, and F. Kong, 2010b: Convection-allowing and convection-parameterizing ensemble forecasts of a mesoscale convective vortex and associated severe weather. *Wea. Forecasting*, **25**, 1052-1081.

Clark, A. J., W. A. Gallus, M. Xue, and F. Kong, 2009: A Comparison of Precipitation Forecast Skill between Small Convection-Allowing and Large Convection-Parameterizing Ensembles. *Wea. Forecasting*, **24**, 1121–1140.

Clark, A. J., S. J. Weiss, J. S. Kain, I. L. Jirak, M. Coniglio, C. J. Melick, C. Siewert, R. A. Sobash, P. T. Marsh, A. R. Dean, M. Xue, F. Kong, K. W. Thomas, Y. Wang, K. Brewster, J. Gao, X. Wang, J. Du, D. R. Novak, F. E. Barthold, M. J. Bodner, J. J. Levit, C. B. Entwistle, T. L. Jensen, and J. Correia Jr., 2012: An overview of the 2010 Hazardous Weather Testbed Experimental Forecast Program Spring Experiment. *Bull. Amer. Meteor. Soc.*, **93**, 55–74.

Corfidi, S. F., J. H. Merritt, and J. M. Fritsch, 1996: Predicting the movement of mesoscale convective complexes. *Wea. Forecasting*, **11,** 41–46.

Dawson, D. T., M. Xue, J. A. Milbrandt, and M. K. Yau, 2010: Comparison of Evaporation and Cold Pool Development between Single-Moment and Multimoment Bulk Microphysics Schemes in Idealized Simulations of Tornadic Thunderstorms. *Mon. Wea. Rev.*, **138**, 1152–1171.

Ebert, E. E., 2001: Ability of a poor man's ensemble to predict the probability and distribution of precipitation. *Mon. Wea. Rev.*, **129,** 2461-2480.

Heideman, K. F., and J. M. Fritsch, 1988: Forcing Mechanisms and Other Characteristics of Significant Summertime Precipitation. *Wea. Forecasting*, **3**, 115–130.

Hu, X. -M., J. W. Nielsen-Gammon, and F. Zhang, 2010: Evaluation of Three Planetary Boundary Layer Schemes in the WRF Model. *J. Appl. Meteor. Climatol.*, **49**, 1831–1844.

Lim, K. -S., and S.-Y. Hong, 2010: Development of an Effective Double-Moment Cloud Microphysics Scheme with Prognostic Cloud Condensation Nuclei (CCN) for Weather and Climate Models. *Mon. Wea. Rev.*, **138**, 1587–1612.

Lin, Y., and K. E. Mitchell, 2005: The NCEP Stage II/IV hourly precipitation analyses: Development and applications. Preprints, *19th Conf. on Hydrology,* San Diego, CA, Amer. Meteor. Soc., 1.2. [Available online at http://ams.confex.com/ams/Annual2005/techprogram/paper_83847.htm.]

Maddox, R. A., C. F. Chappell, and L. R. Hoxit, 1979: Synoptic and meso-alpha aspects of flash flood event. *Bull. Amer. Meteor. Soc.*, **60**: 115-123

Parker, M. D., and R. H. Johnson, 2000: Organizational modes of midlatitude mesoscale convective systems. *Mon. Wea. Rev*, **128,** 3413–3436.

Schumacher, R. S., and R. H. Johnson, 2005: Organization and Environmental Properties of Extreme-Rain-Producing Mesoscale Convective Systems. *Mon. Wea. Rev.*, **133**, 961–976.

Schumacher, R. S., A. J. Clark, M. Xue, and F. Kong, 2013: Factors influencing the development and maintenance of nocturnal heavy-rain-producing convective systems in a storm-scale ensemble. *Mon. Wea. Rev.*, in press.

Thompson, G., R. M. Rasmussen, and K. Manning, 2004: Explicit Forecasts of Winter Precipitation Using an Improved Bulk Microphysics Scheme. Part I: Description and Sensitivity Analysis. *Mon. Wea. Rev.*, **132**, 519–542.

Wang, H., R. Fu, A. Kumar, and W. Li, 2010: Intensification of Summer Rainfall Variability in the Southeastern United States during Recent Decades. *J. Hydrometeor*, **11**, 1007–1018.

Xue, M., F. Kong, K. W. Thomas, Y. Wang, K. Brewster, J. Gao, X. Wang, S. Weiss, A. Clark, J. Kain, M. Coniglio, J. Du, T. Jensen, and Y.-H. Kuo, 2010: CAPS Realtime Storm Scale Ensemble and High Resolution Forecasts for the NOAA Hazardous Weather Testbed 2010 Spring Experiment. 25th Conf. Severe Local Storms, Amer. Meteor. Soc., Paper 7B.3.